FERMILAB-PUB-13-568-AD

Simple lumped circuit model applied to field flatness tuning of 4-rod radio frequency quadrupoles

C.Y. Tan*

Fermi National Accelerator Laboratory,

P.O. Box 500, Batavia, IL 60510-5011, USA.

J.S. Schmidt and A. Schempp

IAP, Goethe University, Frankfurt am Main, Germany.

(Dated: December 11, 2013)

Abstract

The field flatness of any radio frequency quadrupole (RFQ) is an important parameter that needs to be carefully tuned because it can affect beam transmission efficiency. In 4-rod RFQs, the heights of a set of tuning plates determine the quality of the field flatness. The goals of this paper are (a) to show that by using a lumped circuit model of a 4-rod RFQ, the field flatness profile for any tuning plate height distribution can be quickly calculated, (b) to derive a perturbative solution of the model so that insights into the physics of the tuning process and its effects can be understood and (c) to compare the predicted field profiles to measurements.

PACS numbers: 29.20.Ej, 29.27.-a, 29.27.Ac

* cytan@fnal.gov

Operated by Fermi Research Alliance, LLC under Contract No. De-AC02-07CH11359 with the United States Department of Energy.

I. INTRODUCTION

The field flatness (see section II A 1) of any radio frequency quadrupole (RFQ) is an important parameter that needs to be well controlled because it can affect beam transmission efficiency [1]. In the 4-rod RFQ shown in Fig. 1, tuning plates are used to change the voltage in each tuning cell by raising or lowering them. The goal is to move each plate until the field flatness is found that is within some prescribed tolerance, usually $< 5\%$. However, moving the tuning plates also changes the resonant frequency of the RFQ and so the entire process can be quite tedious when this constraint is also included.

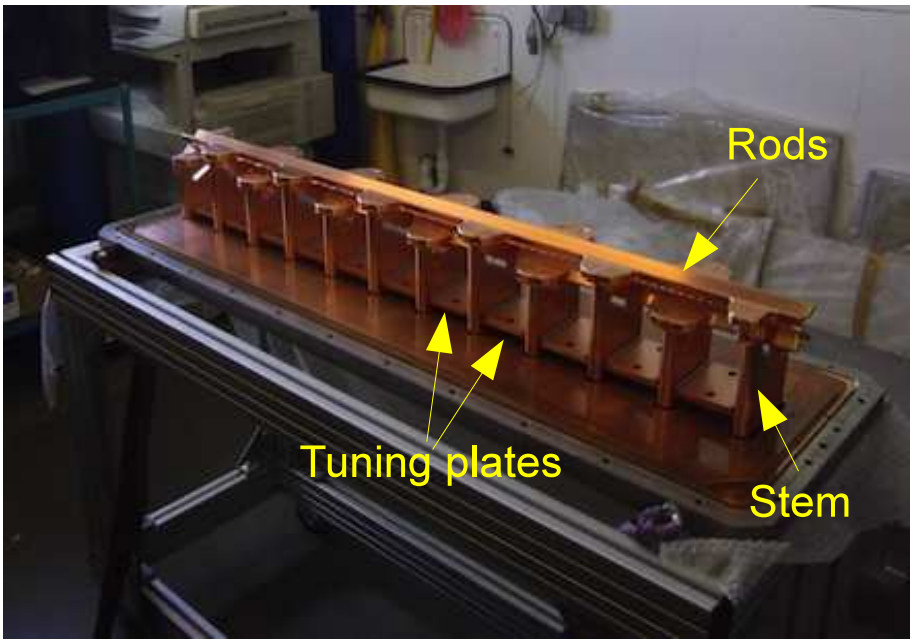

FIG. 1. This picture shows the Fermilab injector RFQ outside of its vacuum tank. The four rods are held by stems and the tuning plates are located between stems. There are 13 tuning cells in this RFQ with 11 full cells and a half cell at each end (for a total of two half cells). The beginning and end cell tuning plates are not installed here. When installed, they go between the vacuum tank wall and the first and last stem.

Historically, the tuning process is done by moving the tuning plates of the RFQ using an iterative trial and error process that can be grossly inefficient [1]. Attempts have been made to semi-automate this process by pre-calculating the tuning plate heights with CST Microwave Studio® (MWS). This simulation tool has been used successfully in the design and tuning for various types of RF accelerators including drift-tube linacs as well as 4-vane

RFQs. However, the agreement between simulation and measurement can be rather poor for 4-rod RFQs [2–5]. An explanation for that could be that the simulation accuracy of MWS is quite different for transmission-line resonators compared to cavity resonators. For example, Fig. 2 presents the results of the MWS field flatness simulation for a fully imported CAD model of the FNAL RFQ. We show here, the results of five models with different meshes that have been refined and varied to improve the simulation accuracy. All of these models have several million mesh cells and all of them exhibit a slope in the simulated field distribution from the low energy end to the high energy end that is not present in our measurement. The deviation between the simulated and measured field flatness in these models can be up to 14%. Similar results have been presented by Kurennoy [5] for the same RFQ. To overcome this problem for particle tracking simulations, a fictive tuning set up that is not the one used in the RFQ is used to reproduce the measured field flatness in simulations. With this field flatness, reasonable particle dynamic simulations can be performed, for example, discussed in reference [5].

Coming back to tuning the RFQ, the lack of an accurate real-time model for the tuning process results in the reversion back to the traditional iterative method.

It is with the above problems in mind that we want to see whether a lumped circuit model of the 4-rod RFQ can be used instead. After we developed this model, we found that the lumped circuit model has at least two advantages: the first is that the solution to the problem essentially becomes an eigenvalue problem that is easily and quickly solved both analytically and numerically. The second is that the fundamental physical relations of the resonator system become more apparent when compared to the 3D-results of detailed models used for MWS simulations.

The idea of modeling a 4-rod RFQ with a lumped circuit model is not new. For example see references [6] and [7] or [8] for its application on a 4-vane RFQ. In this paper, we will use a simplified model for 4-rod RFQs first published by Fang *et al* in 1992 [9] which we will improve and expand upon.

II. THEORY

The motivation behind modeling the RFQ as a series of coupled LC circuits comes from the observation that each tuning cell can be modeled as an LC equivalent circuit. From

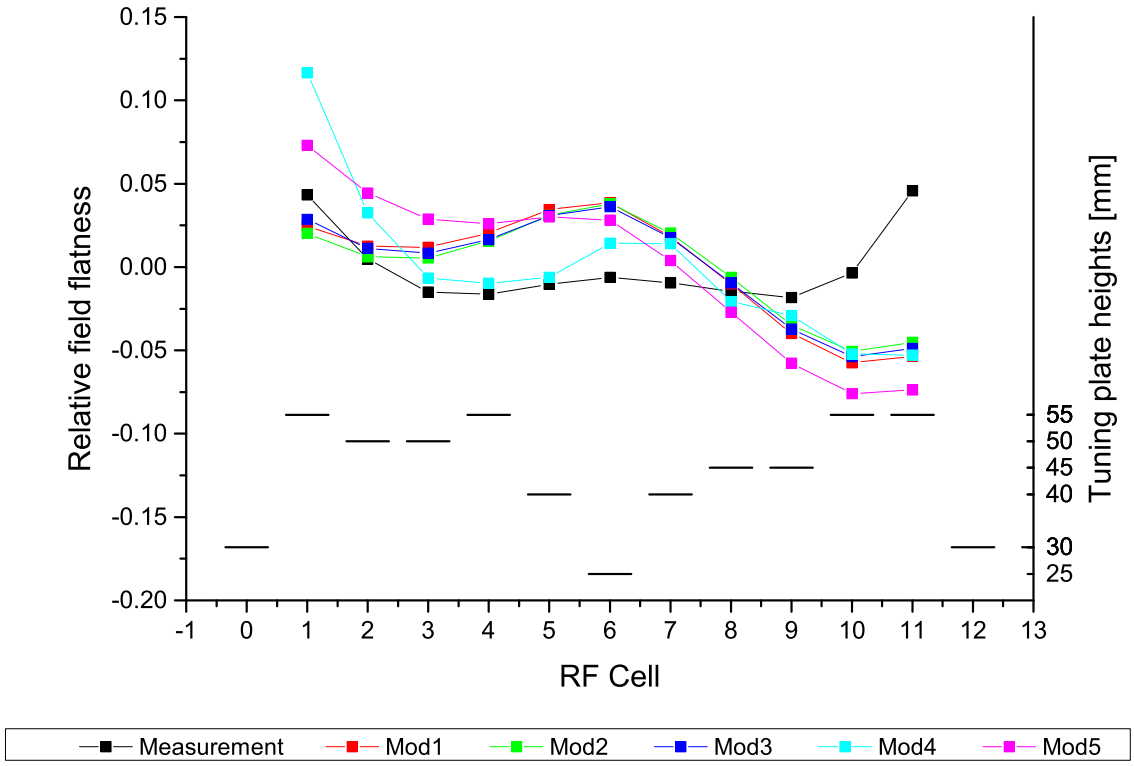

FIG. 2. Comparison of a measured field flatness with its MWS simulation. In this figure, a measured field flatness of the FNAL RFQ (black "■") for a given tuning plate distribution ("–") is compared to the simulation of the fully imported model of this RFQ that has the same tuning set up (Mod1 to Mod5). The simulation models differ in their meshing which has been refined in several steps. All of the simulated field flatness results show a slope from the low energy to the high energy end that is not present in the measurement. The simulated values can deviate up to 14% from the measured value.

Fig. 3, we can see that since there are gaps between the rods, they are capacitively coupled. The stems and the base together allow a current to flow in a loop and thus this structure can be thought of as an inductor. Together, the rods, stems and base form the basic LC circuit for each tuning cell. In order to change the resonant frequency of a cell, a tuning plate is inserted into that cell so that the current path is shortened which, in effect, lowers the inductance of that cell.

Of course, each LC circuit does not live in isolation. In fact, according to Fang, they are

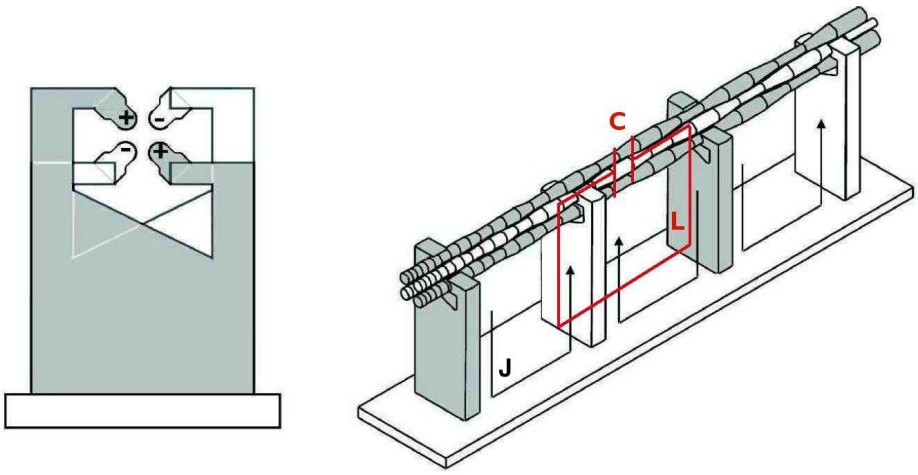

FIG. 3. This is a cartoon of a 4-rod RFQ that has three tuning cells. Each tuning cell can be modeled as an LC circuit with a current J flowing in each cell. Notice that the stems alternatively hold two rods, i.e. the shaded stems hold the shaded rods, while the unshaded stems hold the unshaded rods. The end view of the rod-stem set up shows the quadrupole voltage polarity structure that arises when the currents flow in opposite directions in adjacent tuning cells. This is the necessary quadrupole polarity structure that is required for transverse focusing.

coupled not only to their nearest neighbor but also to their next nearest neighbor. With this in mind, we can create the lumped circuit model of the RFQ shown in Fig. 4. It is important to take into account the direction of the winding of the inductor represented by "•" in the model shown in Fig. 4. In this model, the tuning cells are numbered from $0, \ldots, N$ with cell 0 and N being the half cells. Each tuning cell has capacitance C_n for $n = 0, \ldots, N$ and L_n for $n = 1, \ldots, N-1$, $L_0/2$ for cell 0, and $L_N/2$ for cell N. The coupling between the nearest neighbor cells is $2\kappa_1$ and the next nearest neighbor cells is $2\kappa_2$. It will be seen later when we compare our model to the MWS results, that it is sufficient to have κ_1 and κ_2 independent of cell number.[10] Finally, a current J_n for $n = 0, \ldots, N$ flows in each loop.

Let us examine cell 0 first. We can write down Kirchhoff's equation for it and it is

$$\frac{J_0}{i\omega C_0} + \tfrac{1}{2} i\omega L_0 J_0 - i\kappa_1\omega\sqrt{L_0 L_1} J_1 - i\kappa_2\omega\sqrt{L_0 L_2} J_2 = 0$$

$$\Rightarrow \qquad -J_0\left(1 - \tfrac{1}{2}\omega^2 C_0 L_0\right) - \kappa_1\omega^2\sqrt{L_0 L_1} C_0 J_1 - \kappa_2\omega^2\sqrt{L_0 L_1} C_0 J_2 = 0 \qquad (1)$$

Similarly, we can write down Kirchhoff's equation for the last cell, N, and it is

$$-\kappa_2\omega^2\sqrt{L_{N-2} L_N} C_N J_{N-2} - \kappa_1\omega^2\sqrt{L_{N-1} L_N} C_N J_{N-1} - J_N\left(1 - \tfrac{1}{2}\omega^2 C_N L_N\right) = 0 \qquad (2)$$

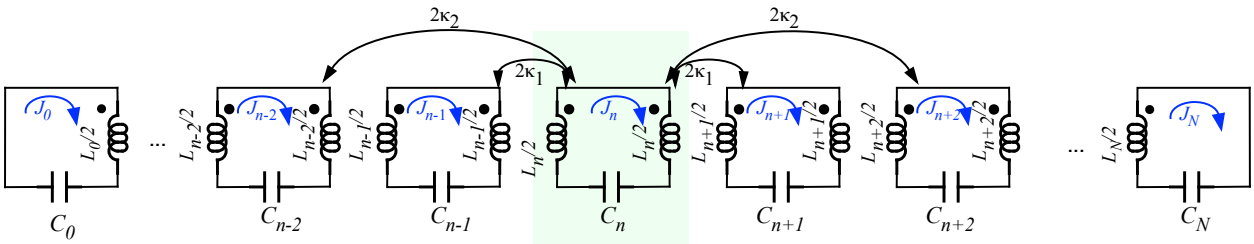

FIG. 4. The RFQ lumped circuit model. The highlighted n'th cell shows how it is coupled to its first and second neighbor circuits. Each closed circuit represents a tuning cell. Notice the "•" that is associated with each inductor. The location of the "•" and the direction of the current determines the sign of the induced voltage that comes from coupling between cells. For an example, see [11].

For any arbitrary cell, n, we have

$$\begin{aligned} &-\kappa_2\omega^2\sqrt{L_{n-2}L_n}C_nJ_{n-2}-\kappa_1\omega^2\sqrt{L_{n-1}L_n}C_nJ_{n-1} \\ &\quad -J_n\left(1-\omega^2L_nC_n\right) \\ &\qquad -\kappa_1\omega^2\sqrt{L_nL_{n+1}}C_nJ_{n+1}-\kappa_2\omega^2\sqrt{L_nL_{n+2}}C_nJ_{n+2}=0 \end{aligned} \tag{3}$$

for $n = 1, \ldots, N-1$. If any subscript is less than zero or greater than N, the term is identically zero. For example, $L_{-1} = J_{-1} = 0$.

A. Eigensystem equation

We can combine Eq. 1, 2 and 3 and turn them into an eigenvector and eigenvalue problem

$$(\boldsymbol{U}_1 - \lambda^2\boldsymbol{I})\boldsymbol{J} = 0 \tag{4}$$

where $\lambda^2 = 1/\omega^2$,

$$\boldsymbol{U}_1 = \begin{pmatrix} m_{0,0}C_0 & m_{0,1}C_0 & m_{0,2}C_0 & 0 & \ldots & \ldots & 0 \\ m_{0,1}C_1 & m_{1,1}C_1 & m_{1,2}C_1 & m_{1,3}C_1 & \ddots & & \vdots \\ m_{0,2}C_2 & m_{1,2}C_2 & \ddots & \ddots & \ddots & \ddots & \vdots \\ 0 & m_{1,3}C_3 & \ddots & \ddots & \ddots & m_{N-3,N-1}C_{N-3} & 0 \\ \vdots & \ddots & \ddots & \ddots & \ddots & m_{N-2,N-1}C_{N-2} & m_{N-2,N}C_{N-2} \\ \vdots & & \ddots & m_{N-3,N-1}C_{N-1} & m_{N-2,N-1}C_{N-1} & m_{N-1,N-1}C_{N-1} & m_{N-1,N}C_{N-1} \\ 0 & \ldots & \ldots & 0 & m_{N-2,N}C_N & m_{N-1,N}C_N & m_{N,N}C_N \end{pmatrix} \tag{5}$$

is a band matrix with

$$\left.\begin{array}{lll} m_{0,0} = \frac{1}{2}L_0, & m_{N,N} = \frac{1}{2}L_N & m_{n,n} = L_n \\ m_{n-1,n} = -\kappa_1\sqrt{L_{n-1}L_n} & m_{n-2,n} = -\kappa_2\sqrt{L_{n-2}L_n} & \end{array}\right\} \quad \text{for } n = 1, \ldots, N-1 \tag{6}$$

and

$$\boldsymbol{J} = \begin{pmatrix} J_0 \\ J_1 \\ J_2 \\ \vdots \\ J_N \end{pmatrix}, \qquad \boldsymbol{I} = \begin{pmatrix} 1 & 0 & \ldots & \ldots & 0 \\ 0 & \ddots & \ddots & & \vdots \\ \vdots & \ddots & \ddots & \ddots & \vdots \\ \vdots & & \ddots & \ddots & 0 \\ 0 & \ldots & \ldots & 0 & 1 \end{pmatrix} \tag{7}$$

It is obvious that if the coupling constants $\kappa_{1,2}$, capacitances $C_{0,\ldots,N}$ and inductances $L_{0,\ldots,N}$ are specified, we can numerically solve Eq. 4 for the eigenmodes and eigenvectors of $\boldsymbol{U}_1$. Note: it is easy to show that the eigenmodes of λ^2 are the same as $1/\lambda^2$.

1. *Definition of field flatness*

We define the voltage V_n in tuning cell n to be

$$V_n = \frac{J_n}{\Omega C_n} \qquad n = 0, \ldots, N \tag{8}$$

where Ω is the resonant frequency of the RFQ. Notice that we have left out the i in Eq. 8 because the relative phase between current and voltage is irrelevant in this application.

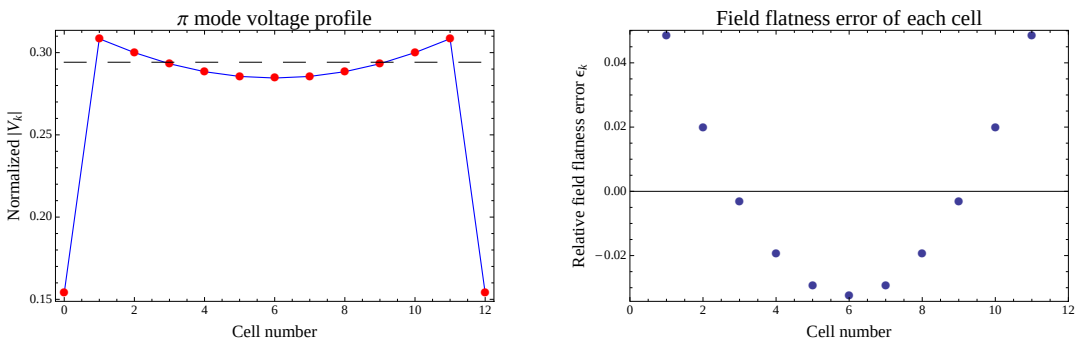

FIG. 5. This is an example of a field profile and error. The dashed line in the graph on the left is $\langle|V|\rangle$ which was defined in section II A 1. In this example, the field error is 8%.

We define the relative field flatness of tuning cell n to be

$$\varepsilon_n = \frac{|V_n| - \langle|V|\rangle}{\langle|V|\rangle} \tag{9}$$

where $\langle |V| \rangle$ is the mean of the absolute voltage in the tuning cells from $n = 1, \ldots, N-1$. Notice that we have left out the end cells in the calculation of the mean because the voltages in these cells tend to be very far from the mean because they are dominated by boundary conditions. And by extension, we define the "normalized" voltage in tuning cell n to be

$$\text{normalized } V_n = \frac{|V_n|}{\sqrt{\sum_{m=1}^{N-1} |V_m|^2}} \tag{10}$$

The field flatness of the RFQ is defined to be the difference between the maximum and minimum relative field flatness found in the list $\{\varepsilon_n |\ n = 1, \ldots, N-1\}$. The goal is to "flatten" this field, i.e. to make the difference as small as possible. An example of a field profile and field flatness error is shown in Fig. 5. This example has been calculated using the parameters shown in Table I, for an ideal 4-rod RFQ that has *no* flaws resulting from manufacture. The curvature that we see here, which we will discuss in section III B 2, is due to $\kappa_2 \neq 0$. So, even in a perfectly manufactured 4-rod RFQ, we may still have to flatten the fields because the field error can be $> 5\%$.

B. Special case

In principle, once we are armed with the eigenvalue equation of the previous section, we can simply fill in the required parameters and numerically calculate the eigenmodes and eigenvectors. However, this defeats one purpose of using the lumped circuit model that is to give us insights into the physics of the tuning process.

The first step in our quest for understanding is to simplify the system. We will set the resonant frequency of each cell to be the same. Thus, if we set $L_n = L$ for $n = 0, \ldots, N$, then it is obvious from Fig. 4 that we must have $C_n = C$ for $n = 1, \ldots, N-1$, and $C_0 = C_N = 2C$. Thus, the $\boldsymbol{U}_1$ matrix becomes

$$\boldsymbol{U}_1 = \lambda_c^2 \begin{pmatrix} 1 & -2\kappa_1 & -2\kappa_2 & 0 & \ldots & \ldots & \ldots & \ldots & 0 \\ -\kappa_1 & 1 & -\kappa_1 & -\kappa_2 & \ddots & & & & \vdots \\ -\kappa_2 & -\kappa_1 & 1 & -\kappa_1 & -\kappa_2 & \ddots & & & \vdots \\ 0 & -\kappa_2 & -\kappa_1 & 1 & -\kappa_1 & -\kappa_2 & \ddots & & \vdots \\ \vdots & \ddots & \ddots & \ddots & \ddots & \ddots & \ddots & \ddots & \vdots \\ \vdots & & \ddots & \ddots & \ddots & \ddots & -\kappa_1 & -\kappa_2 & 0 \\ \vdots & & & \ddots & \ddots & \ddots & 1 & -\kappa_1 & -\kappa_2 \\ \vdots & & & & \ddots & \ddots & -\kappa_1 & 1 & -\kappa_1 \\ 0 & \ldots & \ldots & \ldots & \ldots & 0 & -2\kappa_2 & -2\kappa_1 & 1 \end{pmatrix}$$
$$\equiv \lambda_c^2 \boldsymbol{U}_0(\kappa_1, \kappa_2) \tag{11}$$

where $\lambda_c^2 = 1/\omega_c^2 = LC$. Clearly, $\boldsymbol{U}_1$ is a band matrix and it is not pentadiagonal or symmetric because of the first and last rows.

Next, we set $\kappa_2 = 0$ to see and find analytic solutions for the eigenvalues and eigenvectors of $\boldsymbol{U}_0(\kappa_1, 0)$. Once we find them, we can apply perturbation theory to arrive at a solution for the case when $\kappa_2 \ll \kappa_1$.

1. *Ansatz for finding the eigenvalues and eigenvectors of* $\boldsymbol{U}_0(\kappa_1, 0)$

The clue to finding the eigenvalues and eigenvectors of $\boldsymbol{U}_0(\kappa_1, 0)$ is in its numerical solutions. An example is shown in Fig. 6. From this figure, it is obvious that we can propose

an ansatz for the eigenvectors of $\boldsymbol{U}_0(\kappa_1, 0)$ to have the form

$$\boldsymbol{J}_k = A_k \begin{pmatrix} \cos\frac{0\times k\pi}{N} \\ \cos\frac{1\times k\pi}{N} \\ \cos\frac{2\times k\pi}{N} \\ \vdots \\ \cos\frac{(N-1)\times k\pi}{N} \\ \cos\frac{N\times k\pi}{N} \end{pmatrix} \qquad \text{for } k = 0, \ldots, N \tag{12}$$

where $A_k = 1/\|\boldsymbol{J}_k\|$ and $\|.\|$ is the norm of a vector. It is easy to show that

$$\frac{1}{\|\boldsymbol{J}_k\|} = \begin{cases} \frac{1}{\sqrt{N/2+1}} & \text{if } k \neq 0 \text{ or } k \neq N \\ \frac{1}{\sqrt{N+1}} & \text{if } k = 0 \text{ or } k = N \end{cases} \tag{13}$$

Note: it is interesting that $\boldsymbol{J}_k$ is independent of κ_1.

Let us create a matrix from the column vectors $\boldsymbol{J}_k$

$$\underline{\boldsymbol{J}} = \begin{pmatrix} \boldsymbol{J}_0 & \boldsymbol{J}_1 & \ldots & \boldsymbol{J}_N \end{pmatrix} \tag{14}$$

and after a bit of algebra, we can show that that $\boldsymbol{J}_k$ are the eigenvectors of $\boldsymbol{U}_1(\kappa_1, 0)$ because

$$\underline{\boldsymbol{J}}^{-1}\boldsymbol{U}_0(\kappa_1, 0)\underline{\boldsymbol{J}} = \begin{pmatrix} \Lambda_0 & 0 & \ldots & \ldots & 0 \\ 0 & \Lambda_1 & \ddots & & \vdots \\ \vdots & \ddots & \ddots & \ddots & \vdots \\ \vdots & & \ddots & \ddots & 0 \\ 0 & \ldots & \ldots & 0 & \Lambda_N \end{pmatrix} = \boldsymbol{\Lambda} \tag{15}$$

where $\boldsymbol{\Lambda}$ is a diagonal matrix whose entries $\{\Lambda_k |\ k = 0, \ldots, N\}$ are the eigenvalues of $\boldsymbol{U}_0(\kappa_1, 0)$ and

$$\Lambda_k = 1 - 2\kappa_1 \cos\frac{k\pi}{N} \qquad \text{for } k = 0, \ldots, N \tag{16}$$

Therefore, for $k = N$ which is the π-mode, we can select out the Nth column of $\underline{\boldsymbol{J}}$ and its associated eigenvalue to get

$$\boldsymbol{J}_N = \frac{1}{\sqrt{N+1}} \begin{pmatrix} +1 \\ -1 \\ +1 \\ \vdots \\ (-1)^N \end{pmatrix} \qquad \Omega_N = \frac{\omega_c}{\sqrt{\Lambda_N}} = \frac{\omega_c}{\sqrt{1+2\kappa_1}} \tag{17}$$

where Ω_N is the resonant frequency of the $k = N$ mode.

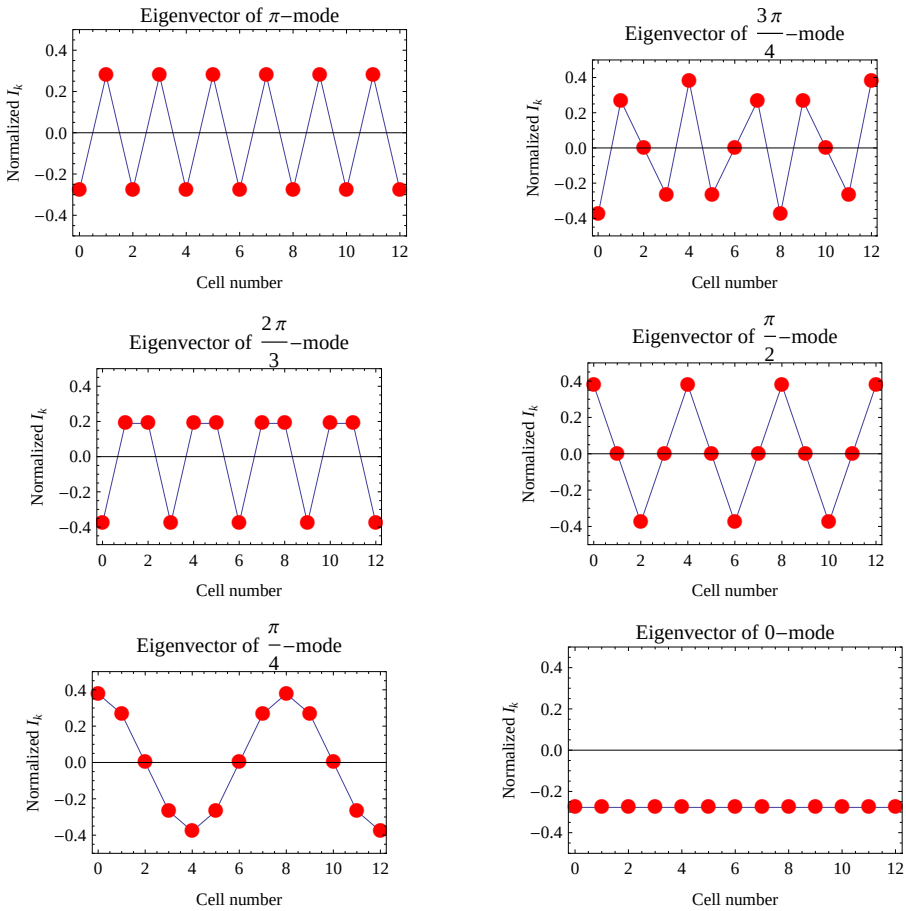

FIG. 6. The normalized eigenvectors of $\boldsymbol{U}_0(\kappa_1, 0)$ plotted in blue and the ansatz plotted as red "•" for a few modes. It is clear that the ansatz matches the numerically calculated eigenvectors exactly.

2. π mode

The reason why the π mode is the required mode for 4-rod RFQs is seen by looking at how the rods are mounted on the stems. It is apparent from Fig. 3 that two rods are held on the same stems that alternate with the stems that hold the other two rods. Therefore, for the rods to have a quadrupole voltage polarity structure, the nearest neighbor tuning cells must have opposite signs in voltage. Hence, the π mode is necessary because it is clear from Eq. 17 that this requirement is satisfied when the currents flow in opposite directions in adjacent cells. MWS simulations shown in appendix C confirm that the currents do flow in opposite directions between adjacent tuning cells for the operating mode which is the π mode.

3. *Application of perturbation theory for finding the eigenvalues and eigenvectors of* $\boldsymbol{U}_0(\kappa_1, \kappa_2)$

We will show how the eigenvalues and eigenvectors are affected by the introduction of the next nearest neighbor coupling κ_2. The first step is to partition $\boldsymbol{U}_0(\kappa_1, \kappa_2)$ into two parts

$$\boldsymbol{U}_0(\kappa_1, \kappa_2) = \boldsymbol{U}_0(\kappa_1, 0) + \begin{pmatrix} 0 & 0 & -2\kappa_2 & 0 & \dots & \dots & \dots & \dots & 0 \\ 0 & 0 & 0 & -\kappa_2 & \ddots & & & & \vdots \\ -\kappa_2 & 0 & 0 & 0 & -\kappa_2 & \ddots & & & \vdots \\ 0 & -\kappa_2 & 0 & 0 & 0 & -\kappa_2 & \ddots & & \vdots \\ \vdots & \ddots & \ddots & \ddots & \ddots & \ddots & \ddots & \ddots & \vdots \\ \vdots & & \ddots & \ddots & \ddots & \ddots & 0 & -\kappa_2 & 0 \\ \vdots & & & \ddots & \ddots & \ddots & 0 & 0 & -\kappa_2 \\ \vdots & & & & \ddots & -\kappa_2 & 0 & 0 & 0 \\ 0 & \dots & \dots & \dots & \dots & 0 & -2\kappa_2 & 0 & 0 \end{pmatrix}$$

$$\equiv \boldsymbol{U}_0(\kappa_1, 0) + \delta\boldsymbol{U}_0(\kappa_2) \tag{18}$$

for $\kappa_2 \ll \kappa_1$. Again, we notice that the first and last rows of $\delta\boldsymbol{U}_0(\kappa_2)$ break its symmetry.

Since the equation that we are going to solve perturbatively is reminiscent of those studied in quantum mechanics (QM), we can, in fact, use the formal perturbation machinery developed in QM to solve our problem. And so in that spirit, we will use the "bra" "ket" notation used in QM to write $\boldsymbol{J}_k$ as an eigenket with eigenvalue Λ_k

$$\boldsymbol{J}_k = |\Lambda_k\rangle \tag{19}$$

However, unlike QM where only Hermitian operators are considered, $\boldsymbol{U}_0(\kappa_1, 0)$ is not symmetric and hence $\{|\Lambda_k\rangle|\ k = 0, \dots, N\}$ is not an orthonormal set. Fortunately, all is not lost, as long as we define the eigenbras $\{\langle\Lambda_k||\ k = 0, \dots, N\}$ properly we can salvage the perturbative technique. The artifice is shown in the appendix A where we find that

$$\langle\Lambda_k| = (\boldsymbol{J}^{-1})_k \tag{20}$$

where $(\boldsymbol{J}^{-1})_k$ is the $(k+1)$'th row of the matrix $\underline{\boldsymbol{J}}^{-1}$. (Note: the exact form of both $\underline{\boldsymbol{J}}$ and $\underline{\boldsymbol{J}}^{-1}$ are shown in appendix B.) And thus, we can have the orthonormality condition satisfied, i.e.

$$\langle\Lambda_k|\Lambda_\ell\rangle = \delta_{k\ell} \tag{21}$$

where $\delta_{k\ell}$ is the Kronecker δ. Thus

$$\langle\Lambda_k|\boldsymbol{U}_0(\kappa_1,0)|\Lambda_k\rangle = \Lambda_k \tag{22}$$

Let us assume that the eigenvector of $\boldsymbol{U}_0(\kappa_1,\kappa_2)$ is $|\Lambda'_k\rangle$ and it can be divided into two parts

$$|\Lambda'_k\rangle = |\Lambda_k\rangle + |\delta\Lambda_k\rangle \tag{23}$$

so that

$$\left.\begin{aligned} \boldsymbol{U}_0(\kappa_1,\kappa_2)|\Lambda'_k\rangle &= \Big[\boldsymbol{U}_0(\kappa_1,0)+\delta\boldsymbol{U}_0(\kappa_2)\Big]\Big[|\Lambda_k\rangle+|\delta\Lambda_k\rangle\Big] \\ &= \Big[\Lambda_k+\delta\Lambda_k\Big]\Big[|\Lambda_k\rangle+|\delta\Lambda_k\rangle\Big] \\ \Rightarrow \qquad \boldsymbol{U}_0(\kappa_1,0)|\delta\Lambda_k\rangle+\delta\boldsymbol{U}_0(\kappa_2)|\Lambda_k\rangle &= \Lambda_k|\delta\Lambda_k\rangle+\delta\Lambda_k|\Lambda_k\rangle \end{aligned}\right\} \tag{24}$$

because in first order perturbation theory, we can neglect the terms $\delta\boldsymbol{U}_0(\kappa_1)|\delta\Lambda_k\rangle$ and $\delta\Lambda_k|\delta\Lambda_k\rangle$. We will assume that $\{|\Lambda_k\rangle|\ k=0,\ldots,N\}$ forms a complete set so that we can write

$$|\delta\Lambda_k\rangle = \sum_{\ell=0}^{N} c_{k\ell}|\Lambda_\ell\rangle \tag{25}$$

where $c_{k\ell}$ are constants to be determined.

When we substitute Eq. 25 into Eq. 24, we have

$$\sum_{\ell=0}^{N} c_{k\ell}\Lambda_\ell|\Lambda_\ell\rangle + \delta\boldsymbol{U}_0(\kappa_2)|\Lambda_k\rangle = \Lambda_k\sum_{\ell=0}^{N} c_{k\ell}|\Lambda_\ell\rangle + \delta\Lambda_k|\Lambda_k\rangle \tag{26}$$

Now, we can apply the orthonormality condition $\langle\Lambda_m|\Lambda_\ell\rangle = \delta_{m\ell}$ from Eq. 21, to Eq. 26 to get

$$c_{km}\Lambda_m + \langle\Lambda_m|\delta\boldsymbol{U}_0(\kappa_2)|\Lambda_k\rangle = c_{km}\Lambda_k + \delta\Lambda_k\delta_{mk} \tag{27}$$

Therefore, the shift in the eigenvalue is found when $m=k$,

$$\delta\Lambda_k = \langle\Lambda_k|\delta\boldsymbol{U}_0(\kappa_2)|\Lambda_k\rangle \tag{28}$$

and the change in eigenvectors is found when $m\neq k$

$$c_{km} = \frac{\langle\Lambda_m|\delta\boldsymbol{U}_0(\kappa_2)|\Lambda_k\rangle}{\Lambda_k-\Lambda_m} \tag{29}$$

Thus using Eq. 25, we have

$$|\delta\Lambda_k\rangle = \sum_{\ell\neq k}^{N}\frac{\langle\Lambda_\ell|\delta\boldsymbol{U}_0(\kappa_2)|\Lambda_k\rangle}{\Lambda_k-\Lambda_\ell}|\Lambda_\ell\rangle \tag{30}$$

where we are allowed to choose $c_{kk}=0$ because $\langle\Lambda'_k|\Lambda'_k\rangle = \langle\Lambda_k|\Lambda_k\rangle = 1$ to first order,

4. Eigenfrequency of π-mode for $\kappa_2 \ll \kappa_1$

The correction to the eigenvalue Λ_k comes from Eq. 28 and is

$$\begin{aligned}\delta\Lambda_k &= \langle\Lambda_k|\delta\boldsymbol{U}_0(\kappa_2)|\Lambda_k\rangle \\ &= (\boldsymbol{J}^{-1})_k\delta\boldsymbol{U}_0(\kappa_2)\boldsymbol{J}_k\end{aligned} \tag{31}$$

For π-mode, we have $k = N$ and when we multiply out Eq. 31, we find that

$$\delta\Lambda_N = -\frac{2\kappa_2(N-1)}{N} \tag{32}$$

We recall that the eigenfrequency Ω_k is related to $\Lambda_k + \delta\Lambda_k$ by

$$\Omega_k = \frac{\omega_c}{\sqrt{\Lambda_k + \delta\Lambda_k}} \tag{33}$$

and so, for π-mode, we have $k = N$ and thus

$$\Lambda_N = 1 + 2\kappa_1 \tag{34}$$

Therefore, the corrected eigenfrequency that takes into account both κ_1 and κ_2 is

$$\Omega_N = \frac{\omega_c}{\sqrt{(1+2\kappa_1) - 2\kappa_2(N-1)/N}} \tag{35}$$

5. Eigenvector correction of π-mode eigenvector for $\kappa_2 \ll \kappa_1$

The correction to the eigenvector $|\Lambda_k\rangle$ comes from Eq. 30 and is

$$\begin{aligned}|\delta\Lambda_k\rangle &= \sum_{\ell\neq k}^{N} \frac{\langle\Lambda_\ell|\delta\boldsymbol{U}_0(\kappa_2)|\Lambda_k\rangle}{\Lambda_k - \Lambda_\ell}|\Lambda_\ell\rangle \\ &= \sum_{\ell\neq k}^{N} \frac{(\boldsymbol{J}^{-1})_\ell\delta\boldsymbol{U}_0(\kappa_2)\boldsymbol{J}_k}{\Lambda_k - \Lambda_\ell}\boldsymbol{J}_\ell\end{aligned} \tag{36}$$

We notice that

$$(\boldsymbol{J}^{-1})_\ell\delta\boldsymbol{U}_0(\kappa_2)\boldsymbol{J}_N \propto \kappa_2 \tag{37}$$

because $\boldsymbol{J}_k$ is independent of both κ_1 and κ_2, and from Eq. 16, we have

$$\Lambda_N - \Lambda_\ell = \begin{cases} 2\kappa_1\left(1 + \cos\frac{\ell\pi}{N}\right) & \text{if } \ell \neq 0 \\ 4\kappa_1 & \text{if } \ell = 0 \end{cases} \tag{38}$$

Therefore,

$$\frac{(\boldsymbol{J}^{-1})_\ell \delta \boldsymbol{U}_0(\kappa_2)\boldsymbol{J}_N}{\Lambda_N - \Lambda_\ell} \propto \frac{\kappa_2}{\kappa_1} \quad \Rightarrow |\delta\Lambda_N\rangle \propto \frac{\kappa_2}{\kappa_1} \equiv \mu \tag{39}$$

Hence, we have demonstrated that as long as μ remains constant, the correction $|\delta\Lambda_N\rangle$ remains constant, and this is the reason why the curvature that will be shown later in Fig. 9 remains the same when κ_1 is changed while keeping μ constant.

C. The effect of changing the height of any tuning plate

The effect on the eigenfrequencies and eigenvectors for arbitrary tuning plate positions will be studied in this section. Let us denote the height of the tuning plate in cell n to be h_n and when all the tuning plates are at their lowest position, i.e. $h_n = 0$, the inductance $L_n = L$ for $n = 0, \ldots, N$, and the capacitance for cells $n = 1, \ldots, N-1$ is $C_n = C$ and $C_0 = C_N = 2C$. Now, unlike in previous sections, we must allow for arbitrary heights h_n (see Fig. 7). This means that the inductance in cell n becomes

$$L_n \to L + \delta L_n \tag{40}$$

where δL_n is the change in inductance in cell n from L.

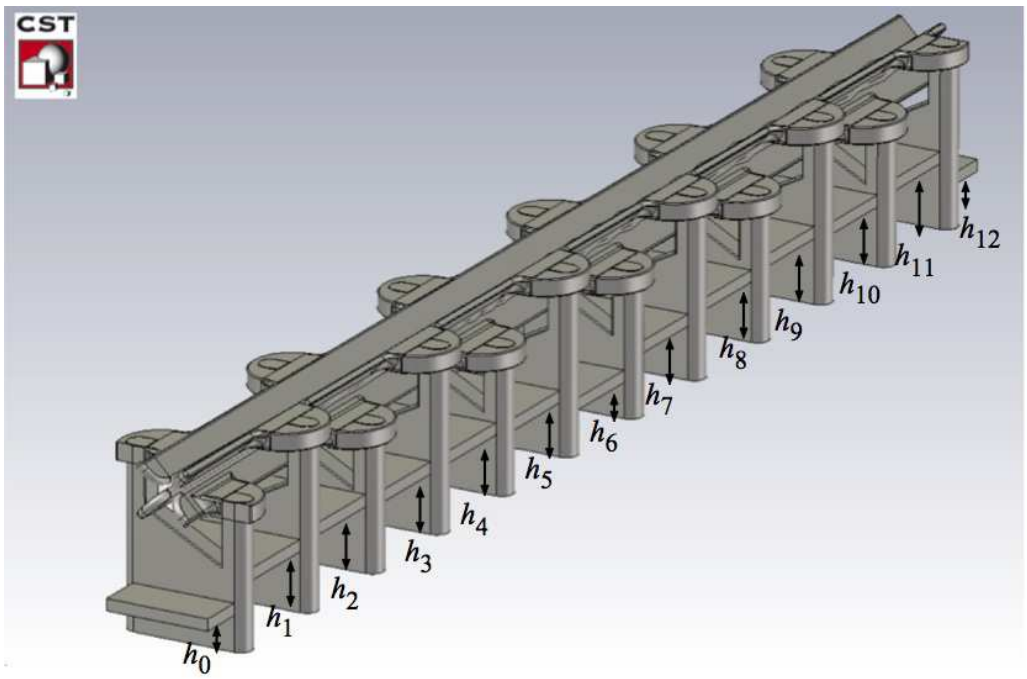

FIG. 7. This is a view of the Fermilab RFQ that shows the tuning plates at arbitrary heights h_n.

From Eq. 5, we have two types of terms to consider. The first type comes from the diagonal of $\boldsymbol{U}_1$ which is

$$L_n C_n = (L + \delta L_n)C \Rightarrow L_n C_n = LC\left(1 + \frac{\delta L_n}{L}\right) \tag{41}$$

We can write the above in terms of the base cell frequency $\omega_c^2 = 1/LC$ and the new base frequency ω_n'

$$\begin{aligned} \omega_n' &= \frac{\omega_c}{\left(1 + \frac{\delta L_n}{L}\right)^{1/2}} \approx \omega_c\left(1 - \tfrac{1}{2}\frac{\delta L_n}{L}\right) \quad \text{for } \delta L_n \ll L \\ \Rightarrow \qquad \frac{\delta L_n}{L} &= -\frac{2(\omega_n' - \omega_c)}{\omega_c} \equiv -\delta_n \end{aligned} \tag{42}$$

The advantage of using frequency changes rather than inductance changes when populating the entries of $\boldsymbol{U}_1$ is that the form of $\boldsymbol{U}_1$ remains unchanged when the C_n's are perturbed.

Therefore, $L_n C_n$ in terms of the base cell frequency ω_c and its shift δ_n is

$$L_n C_n = \frac{1}{\omega_c^2}\left(1 - \delta_n\right) \tag{43}$$

The second type comes from the off-diagonal of $\boldsymbol{U}_1$ which is

$$\begin{aligned} \sqrt{L_n L_m}C &= \sqrt{(L + \delta L_n)(L + \delta L_m)}C \\ &\approx LC\sqrt{\left(1 + \frac{\delta L_n}{L}\right)\left(1 + \frac{\delta L_m}{L}\right)} \\ &= \frac{1}{\omega_c^2}\left[1 - \tfrac{1}{2}\left(\delta_n + \delta_m\right)\right] \\ &\equiv \frac{1}{\omega_c^2}\left(1 - \tfrac{1}{2}\Delta_{nm}\right) \end{aligned} \tag{44}$$

where we have neglected the $(\delta L_n)(\delta L_m)/L^2$ term.

When we substitute Eq. 43 and 44 into Eq. 5, we have

$$\boldsymbol{U}_1 = \lambda_c^2\Big[\boldsymbol{U}_0(\kappa_1, 0) + \delta\boldsymbol{U}_0(\kappa_2) + \delta\boldsymbol{W}_0(\kappa_1, \kappa_2)\Big] \tag{45}$$

where

$$\delta \boldsymbol{W}_0 = \begin{pmatrix} -\delta_0 & \kappa_1\Delta_{0,1} & \kappa_2\Delta_{0,2} & 0 & \dots & \dots & \dots & \dots & 0 \\ \frac{\kappa_1}{2}\Delta_{0,1} & -\delta_1 & \frac{\kappa_1}{2}\Delta_{1,2} & \frac{\kappa_2}{2}\Delta_{1,3} & \ddots & & & & \vdots \\ \frac{\kappa_2}{2}\Delta_{0,2} & \frac{\kappa_1}{2}\Delta_{1,2} & -\delta_2 & \frac{\kappa_1}{2}\Delta_{2,3} & \frac{\kappa_2}{2}\Delta_{2,4} & \ddots & & & \vdots \\ 0 & \ddots & \ddots & \ddots & \ddots & \ddots & \ddots & & \vdots \\ \vdots & \ddots & \ddots & \ddots & \ddots & \ddots & \ddots & \ddots & \vdots \\ \vdots & & \ddots & \ddots & \ddots & \ddots & \ddots & \frac{\kappa_2}{2}\Delta_{N-3,N-1} & 0 \\ \vdots & & & \ddots & \ddots & \ddots & -\delta_{N-2} & \frac{\kappa_1}{2}\Delta_{N-2,N-1} & \frac{\kappa_2}{2}\Delta_{N-2,N} \\ \vdots & & & & \ddots & \ddots & \ddots & -\delta_{N-1} & \frac{\kappa_1}{2}\Delta_{N-1,N} \\ 0 & \dots & \dots & \dots & \dots & 0 & \kappa_2\Delta_{N,N-2} & \kappa_1\Delta_{N,N-1} & -\delta_N \end{pmatrix} \tag{46}$$

Now, we can apply exactly the same methods discussed in section II B using perturbation theory to calculate the effect of changes in L_n. The correction to the eigenvalues Λ_k comes from Eq. 28 and is

$$\delta\Lambda_k = (\boldsymbol{J}^{-1})_k \Big[\delta \boldsymbol{U}_0(\kappa_2) + \delta \boldsymbol{W}_0(\kappa_1, \kappa_2)\Big] \boldsymbol{J}_k \tag{47}$$

and the correction to the eigenvectors comes from Eq. 30

$$|\delta\Lambda_k\rangle = \sum_{\ell\neq k}^{N} \frac{(\boldsymbol{J}^{-1})_\ell \Big[\delta \boldsymbol{U}_0(\kappa_2) + \delta \boldsymbol{W}_0(\kappa_1, \kappa_2)\Big] \boldsymbol{J}_k}{\Lambda_k - \Lambda_\ell} \boldsymbol{J}_\ell \tag{48}$$

We will compare these perturbative solutions to the numerical solution of the same eigensystem in section IV.

If we continue further, and after quite a bit of expansion and simplification of Eq. 48, we find that when only the n'th plate is moved, the correction when expanded to first order in δ_n is

$$\sum_{\ell\neq k}^{N} \frac{(\boldsymbol{J}^{-1})_\ell \delta \boldsymbol{W}_0(\kappa_1, \kappa_2) \boldsymbol{J}_k}{\Lambda_k - \Lambda_\ell} \boldsymbol{J}_\ell = \delta_n \sum_{\ell\neq k}^{N} w_\ell(\kappa_1, \kappa_2, n) \boldsymbol{J}_\ell \tag{49}$$

where w_ℓ are functions independent of δ_n. The above relationship turns out to be important for understanding and explaining the idiosyncrasies of the superposition method that has been historically used to predict the field profile. For example, it can be shown using Eq. 49 that the H function mentioned in references [3] and [12] is, in fact, δ_n.

Furthermore, by linearizing the problem, we have made methods such as Gauss-Newton available to us for the optimization of either L_n or C_n (in the form of δ_n) to fit to simulated or measured eigenvectors.

III. USING THE MODEL

In order to use our model, we must calculate L_n, C_n, κ_1, κ_2 and $\delta L_n/L$ using the results from MWS and then refine these values by using the results from measurements. The Fermilab RFQ will serve as the structure for this exercise [13]. Before we begin, we need to discuss the duality of L_n and C_n. Duality helps by allowing us to keep either L_n or C_n constant and then varying the remaining variable for fitting purposes.

A. Duality of L_n and C_n

We notice that the natural frequency of each *isolated* tuning cell is $\omega'_n = 1/\sqrt{L_n C_n}$ for $n = 1, \ldots, N-1$, $\omega'_0 = 1/\sqrt{L_0 C_0/2}$ and $\omega'_N = 1/\sqrt{L_N C_N/2}$, i.e.

$$\omega_n'^{\,2} \propto \frac{1}{L_n C_n} \qquad \text{for } k = 0, \ldots, N \tag{50}$$

We can think of L_n and C_n as mathematical duals because any variation of the tuning cell from the ideal can either be assigned as an error to either L_n or C_n.

B. Fits to MWS data

In the first pass, we will assume that $C_n = C$ for $n = 1, \ldots, N-1$, $C_0 = C_N = 2C$ to allow us to calculate κ_1, κ_2 and $\delta L_n/L$ by fitting the model to the MWS results. In the second pass, where we have to match our model to the measured field flatness, we will vary the capacitance of each cell to get a good fit. Note: the MWS model of the RFQ used in this section does not contain any modulations and so the field flatness profile will be symmetric about cell 6 when all the tuning plates are at the same height.

1. *Value of C*

We have to set some value to C in order to get the ball rolling. There are several ways to calculate the capacitance of the system with simplified electrodes in the form of circular rods. The solution to these models are typically derived with the theory of cables or image charges, like the examples given in [14]. Instead of using these simplified models, we have simulated the capacitance of the electrodes using CST EM Studio® (EMS). EMS exports a

TABLE I. Lumped Circuit Model Parameters

Parameter	**Value**	**Units**	**Description**
$N+1$	13		number of tuning cells
C	8.3	pF	$C_n = C$ for $n = 1, \ldots, N-1$, $C_0 = C_N = 2C$
L	0.108	μH	$L_n = L$ for $n = 0, \ldots, N$
κ_1	0.0936		first neighbor coupling
κ_2	0.0031		second neighbor coupling
a	-1.00×10^{-6}	mm^{-2}	coefficient of h^2 in $\delta L(h)/L$
b	-0.38×10^{-4}	mm^{-1}	coefficient of h in $\delta L(h)/L$

capacitance matrix of the system which includes the separated lumped capacitance between each defined potential as shown in Fig. 8.

According to the quad star model, also shown in Fig. 8, we can describe the quadrupole as a capacitance C_A, consisting of the four parallel capacitors c_{ij} between the electrodes,

$$C_A = c_{12} + c_{23} + c_{34} + c_{41} \tag{51}$$

and are in series with two capacitors C_B and C_C

$$\begin{aligned} C_B &= c_{11} + c_{33} \\ C_C &= c_{22} + c_{44} \end{aligned} \tag{52}$$

C_B and C_C represent the capacitance between two pairs of electrodes $(V1, V3)$, $(V2, V4)$ and the boundary.

These capacitors C_A, C_B and C_C form a π-network as one can find for example in [14] and with $V1 = V3 = -V2 = -V4$ it leads to a capacitance of the electrodes C_T described by

$$C_T = C_A + \frac{C_B C_C}{C_B + C_C} \tag{53}$$

When we substitute the values, given in the capacitance matrix of EMS, into Eq. 51, 52 and 53, we find that $C_T = 124.6$ pF and thus the lumped circuit capacitance $C = C_T/15 = 8.3$ pF because the total capacitance of the RFQ lumped circuit model is $C_T = 11C + 2 \times 2C = 15C$.

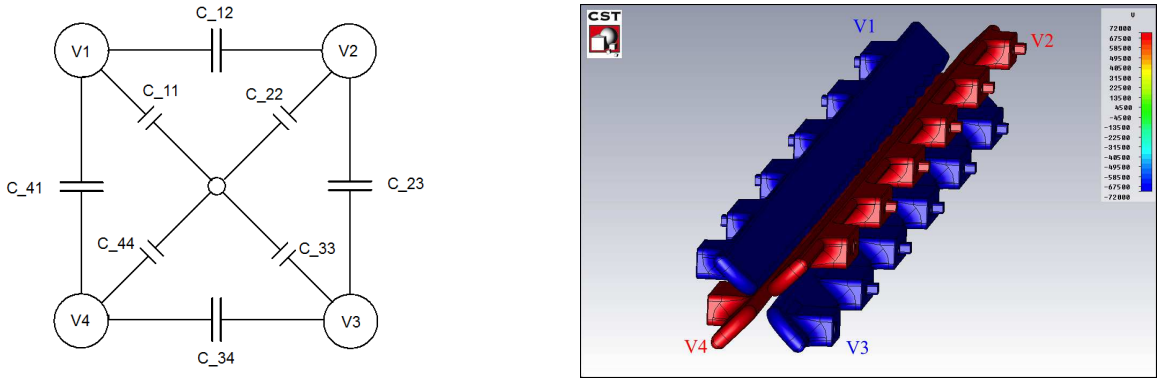

FIG. 8. For the purpose of calculating C with EMS, we have set one pair of electrodes to 72 kV (red) and another pair to -72 kV (blue). From here, we can extract the lumped capacitance matrix to calculate C_T using the star quad model.

2. *Extracting κ_1 and κ_2*

We can extract κ_1 and $\kappa_2 = \mu\kappa_1$ by using the MWS results for the case when all the tuning plates are at zero. In addition, we will also keep the resonant frequency fixed at 154.733 MHz found by MWS in this configuration. The goal is to perform a least square fit to minimize the difference between the π-mode eigenvector $\boldsymbol{J}_{12}$ and the MWS eigenvector by varying κ_1 and μ with the given constraint.

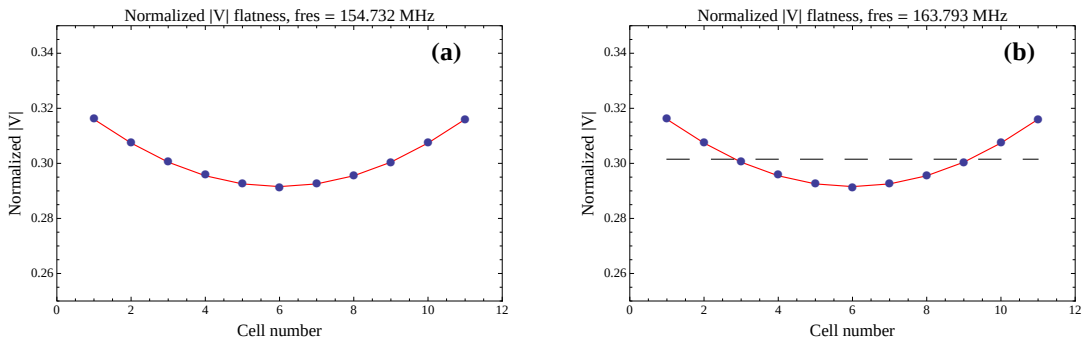

FIG. 9. (a) The red curve is the result of fitting the model to the MWS field flatness profile (blue "•") while keeping the resonant frequency fixed. (b) κ_1 is increased by 10× while μ has the same value that is used to create (a). The curve from (a) is still good but the resonant frequency has shifted. The dashed line represents the case when $\mu = 0$ and shows that there is no curvature in this case.

The results of the fit are $\kappa_1 = 0.0936$ and $\mu = 0.03351$ and are shown in Fig. 9(a). We also illustrate in Fig. 9(b) that when $\kappa_1 \to (10 \times \kappa_1 = 0.936)$ but with μ kept constant, the fit remains good, but the resonant frequency has changed to 163.793 MHz. This result supports the point that was made earlier in section II B 5 and Eq. 39 that to first order, κ_1 determines the resonant frequency while μ determines the curvature of the field.

As a consequence of the choice of C and the fit, $L = 0.108$ μH when the above values are substituted into Eq. 35. Table I summarizes all the results of the fits to the MWS data.

3. *Constructing δL as a function of h*

The resonant frequency change of the RFQ when all its tuning plates are raised to the same height, shown in Fig. 10, indicates to us that δL must be at least a quadratic function of the tuning plate height h. Therefore, let us define two free parameters a and b in the following equation

$$\delta L(h) = L(ah^2 + bh) \tag{54}$$

that will be found by fitting to the MWS data described below. Reminder: we have assumed that $\delta L(h)$ is the same for all tuning cells.

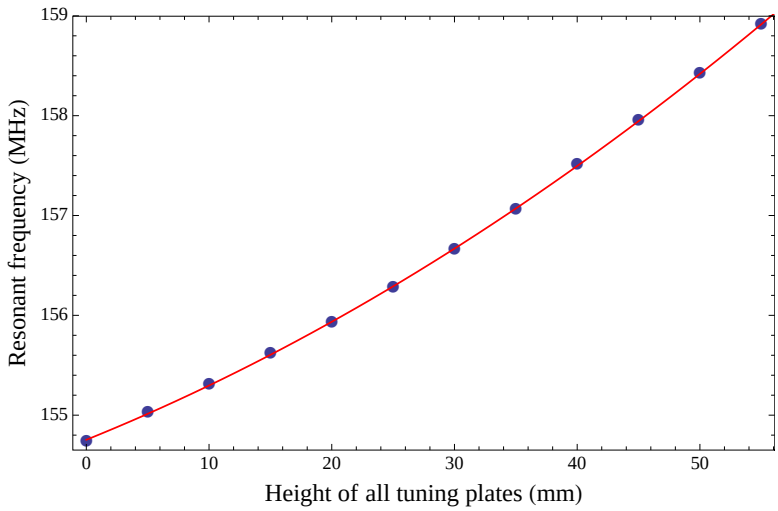

FIG. 10. The resonant frequency when all the tuning plates are raised to the same height calculated by MWS. When all the tuning plates are at 0 mm, the resonant frequency is 154.7 MHz and 158.4 MHz at 50 mm. The red curve is a quadratic fit to the data.

We choose to find a and b by applying a least squares fit that minimizes the difference

between the model relative voltage, $|V_3(h_3)/V_3(0)|$, and the same ratio found by MWS. We define $V_3(h_3)$ to be the voltage in cell 3 when the tuning plate is at h_3 while all the other tuning plates are at zero height. The fit gives

$$a = -1.00 \times 10^{-6}\ \mathrm{mm}^{-2} \qquad b = -0.38 \times 10^{-4}\ \mathrm{mm}^{-1} \tag{55}$$

and Fig. 11(a) shows the result of the least squares fit plotted with the MWS data. The range of $\delta L(h)/L$ is much smaller than expected and it has the consequence that the resonant frequency is not predicted correctly as a function of tuning plate height. This easily shown when we use Eq. 42 and the values of the resonant frequencies from Fig. 10

$$\frac{\delta L}{L} = -\frac{2(f_{\mathrm{res}}(50) - f_{\mathrm{res}}(0))}{f_{\mathrm{res}}(0)} = -\frac{2(158.4 - 154.7)}{154.7} = -0.048 \tag{56}$$

where $f_{\mathrm{res}}(h)$ is the resonant frequency calculated by MWS when all the plates are at h mm. However, when we substitute the a and b values in Eq. 55 into Eq. 54, we get $\frac{\delta L}{L} = -0.0044$ which is 10× smaller than what we expect. This is a weakness of the model that will need to be addressed in the future.

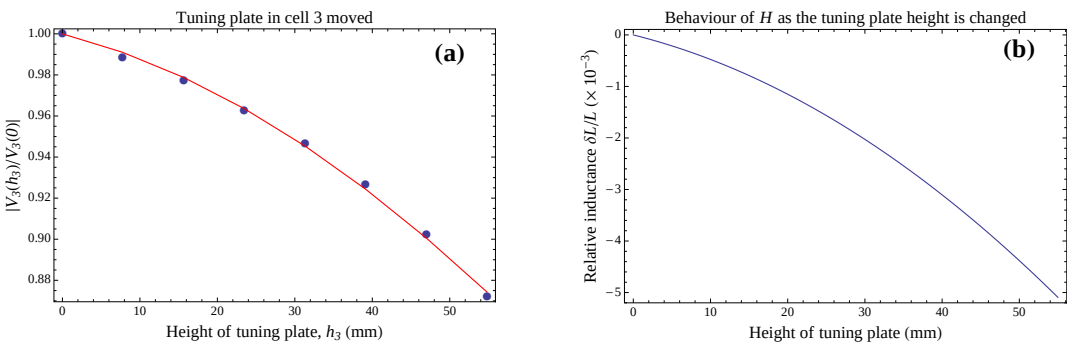

FIG. 11. (a) The red curve is the result of fitting the model to the MWS data (blue "•") when tuning plate 3 is moved. (b) is the corresponding $\delta L/L$ found from the fit. See text.

IV. COMPARISON OF THE MODEL TO THE MWS RESULTS

As a comparison, we can apply our model with the parameters found in the previous sections and summarized in Table I to other MWS results. Fig. 12 shows a selection of MWS data that are plotted against the predicted curves of our model by numerically solving the eigensystem given by Eq. 5 and by perturbation theory described in section II B 3. We

can see that the predicted curves of both numerical solution and the perturbation solution can match the MWS data quite well. However, clearly, both methods do not always match the MWS data exactly. Sometimes, one method seems to be better than the other. The discrepancies are highlighted in the caption of that figure. We can certainly make the curves fit better to the MWS data by varying the capacitance of each cell but this effort is better expended on fitting the curves to measured data. This will be the topic of the next section.

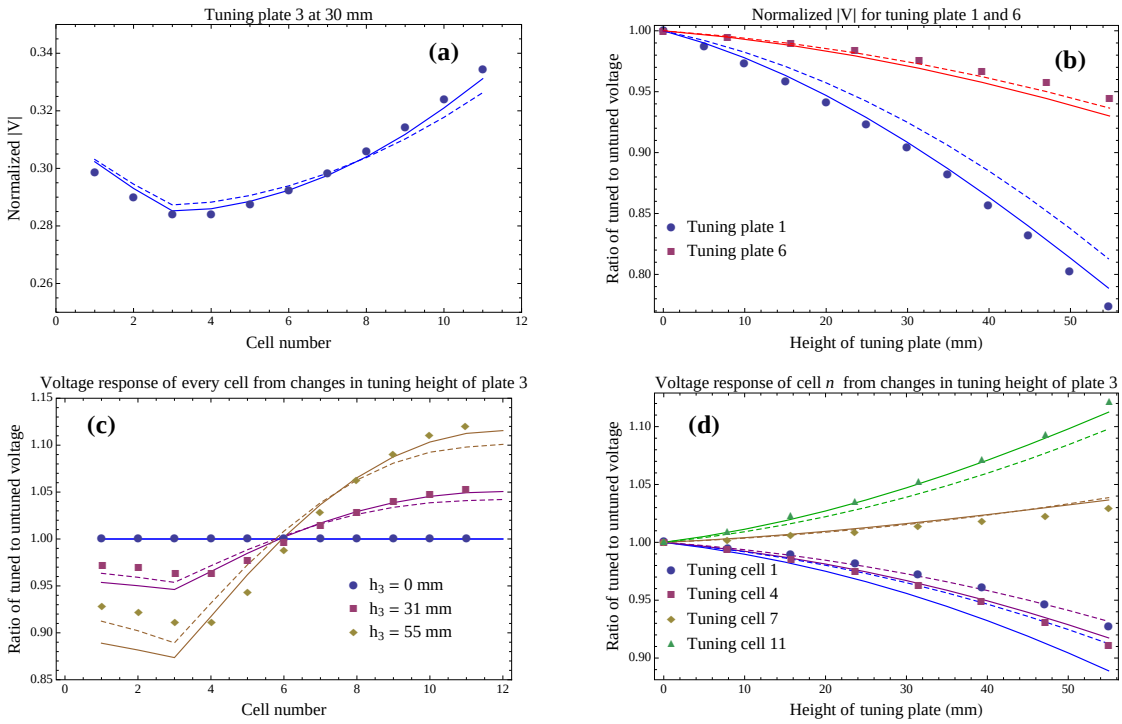

FIG. 12. All the curves have been calculated using the parameters shown in Table I and the "•", "■", etc. come from MWS. All the continuous curves come from numerically solving Eq. 4 and the dashed curves come from perturbation theory solutions described in section II B 3. (a) The relative field flatness when tuning plate 3 is at 30 mm while the rest are at 0 mm. (b) The relative voltage in tuning cells 1 and 6 when their tuning plates are moved (c) The relative field flatness of all the cells when the tuning plate in cell 3 is set to 31 mm and 55 mm. The predicted curves are good for tuning cells 4 to 11. Interestingly, the perturbative solution matches the MWS data better than the numerical eigensytems solution. (d) The relative voltage response of tuning cells 1, 4, 7 and 11 when tuning plate 3 is moved. The predicted curves using the numerical eigensystems method match the MWS data very well except for cell 1, while the perturbative solution does not do as well.

V. FITTING THE MODEL TO MEASURED RESULTS

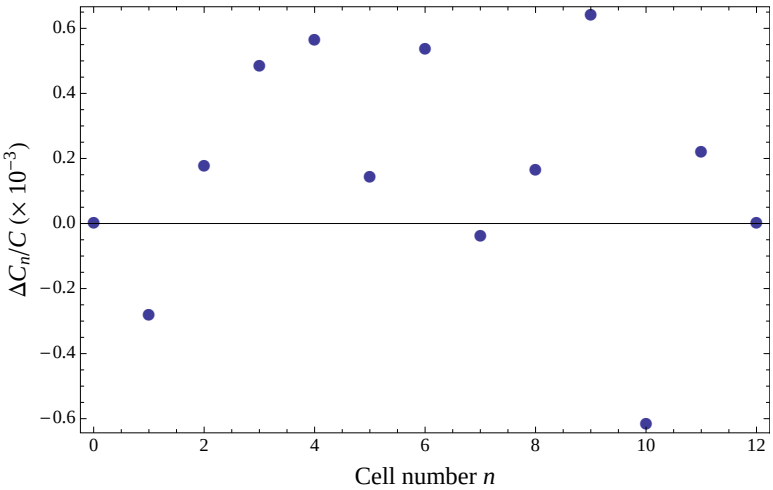

FIG. 13. The relative change $\Delta C_n/C$ for $n = 1, \ldots, 11$ that are needed to minimize the difference between the predicted relative voltage and the measurements when tuning plates 3 and 9 are individually set to 20 mm. The results of the fit are shown in Fig. 14. Note: we did not use the effect of tuning plates 0 and 12 in the fits.

The list of capacitance corrections that are needed for the model to fit to the measured relative voltage [15] is $\Delta \boldsymbol{C} = \{\Delta C_n |\ n = 0, \ldots, 12\}$. We will only consider the cases where tuning plates 3 and 9 have been set to 20 mm because we want to determine whether our fit to a subset of the data set is sufficient to predict the voltage behavior when applied to the remaining data set. Fig. 13 shows the $\Delta \boldsymbol{C}$ required for fitting to this subset. Note: we have left out the voltage effects of tuning plates 0 and 12 because we did not measure their effects.

The results presented in Fig 14 illustrate that the relative changes to the capacitance are asymmetric about tuning cell 6 and are very small when compared to C. We believe that both the asymmetry and $\Delta C_n \ll C$ indicate the influence of the growing modulation [2] and to second order, the manufacturing and mounting errors of the rods.

The model predictions using $\Delta \boldsymbol{C}$ are shown in Fig. 14. When we compare the predicted results to the measurements, we see that the model and measurements match extremely well. These results set us up for comparing the model with these parameters to the measurements for arbitrarily set tuning plate heights. This will be discussed in the next section.

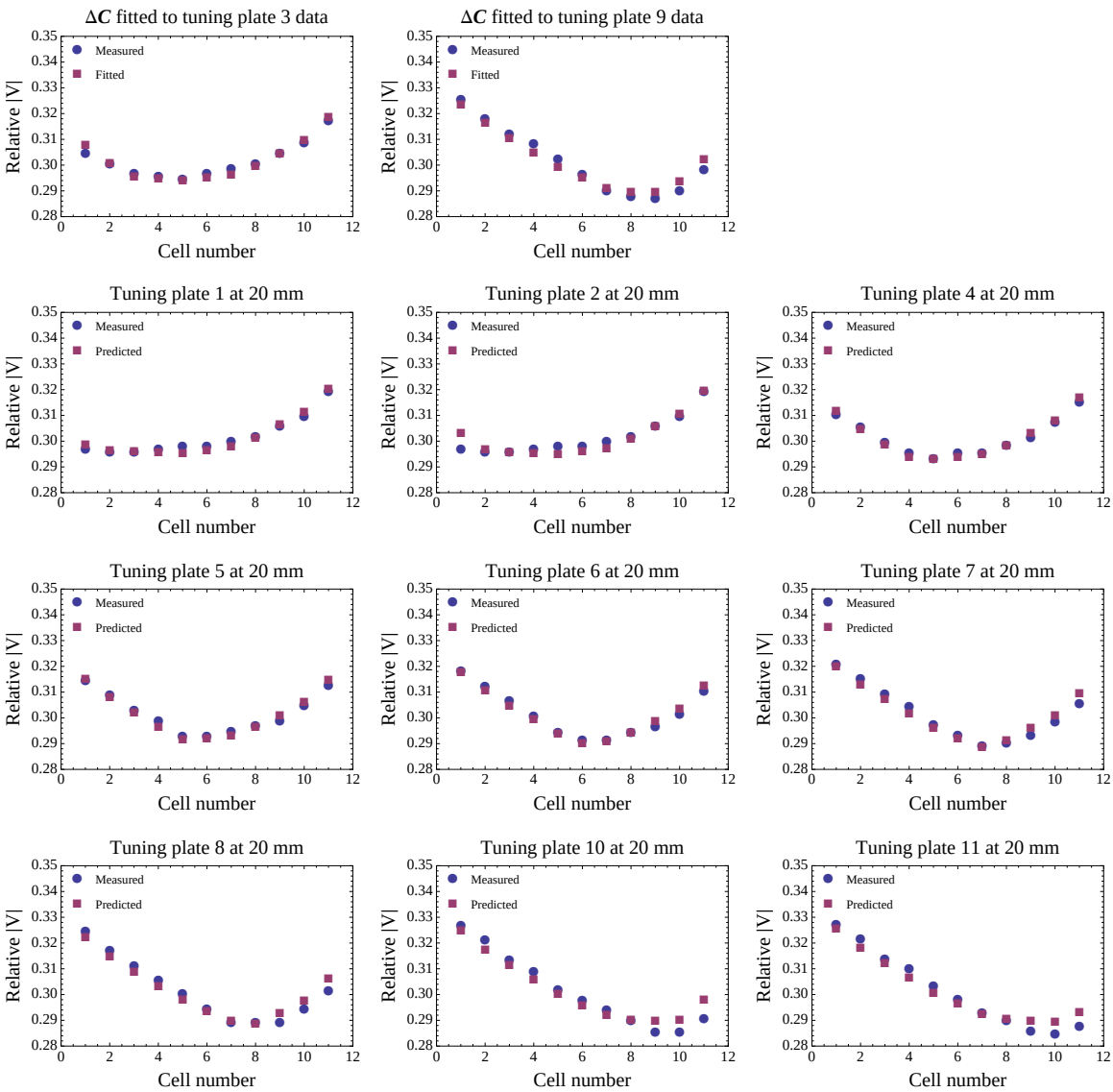

FIG. 14. We fit $\Delta \boldsymbol{C}$ to the measured relative field profile for the cases when the tuning plates in cells 3 and 9 were set to 20 mm. We then used the $\Delta \boldsymbol{C}$ that we found (see Fig. 13) and applied it to the model. The results are plotted here for the other cells when each plate was raised to 20 mm. We can see that the predicted relative voltage and the measured relative voltage match extremely well.

VI. COMPARISON OF THE MODEL PREDICTED FIELD FLATNESS TO MEASUREMENT

In this section, we will compare our model prediction to measurements by the simple and direct way of numerically solving the eigensystem equation derived in section II A after filling in $\boldsymbol{U}_1$ with the values from Table I, $\delta L_n/L$ and $\Delta\boldsymbol{C}$ found in the previous sections. We will not delve into detail about how to accomplish the extraction of the eigenvectors of $\boldsymbol{U}_1$ because many canned packages are able to do this easily. The model predictions compared to three measurements with arbitrary tuning plate heights are shown in Fig. 15.

In order to test the hypothesis that results of the model can predict the measurements, we will use the reduced χ^2 goodness of fit test.[16] The definition of the reduced χ^2 is

$$\chi^2/\nu = \frac{1}{\nu}\sum_{n=1}^{11}\frac{(\tilde{V}_{\text{measured}}(n) - \tilde{V}_{\text{predicted}}(n))^2}{\sigma_n^2} \tag{57}$$

where $\tilde{V}_{\text{measured}}(n)$ and $\tilde{V}_{\text{predicted}}(n)$ are the measured relative voltage and the predicted relative voltage in cell n respectively, σ_n^2 is the variance of the measurement in cell n and ν is the number of degrees of freedom.

In all the example setups, ν = number of tuning plates = 11 because we are not fitting or deriving any statistical quantities from the measurements. When we choose the significance value $\alpha = 0.05$, the critical value $\chi^2/\nu_{\text{crit}} = 1.78$. We will use χ^2/ν_{crit} to determine whether the models acceptably describe the measurements. And for calculating χ^2/ν, we will assume that the measurements have a standard error of 1%.

For setup 1, where most of the tuning plate heights are close to 20 mm, $\chi^2/\nu = 0.24$ of our model is $< \chi^2/\nu_{\text{crit}}$, and so we do not reject our models at the 5% significance level. We can see by eye that the model predictions do indeed match the measurements very well.

For setup 2, we have raised most of the tuning plates to about 50 mm. Again, the model $\chi^2/\nu = 0.88 < \chi^2/\nu_{\text{crit}}$ and so we do not reject this model at the 5% significance level.

For setup 3, we see that the model does not match the measurements very well at the 5% significance level because $\chi^2/\nu = 11.9 > \chi^2/\nu_{\text{crit}}$. However, the shape of the prediction correlates with the measurements. This indicates that $\Delta\boldsymbol{C}$ needs further refinement.

Therefore, from these three setups, we can see that our model is usable for predicting the shape of the field profile. And for two of our three setups, the model predictions match the measurements. In fact, in practice, we can imagine after each setup and measurement,

the value of the capacitance used for each cell can be refined to make the predicted profile match the measured profile. Then, with the new set of capacitances, we can use it to predict the next profile for a new set of tuning plate heights. These iterations that consist of the sequence of prediction and correction form the basis of a tuning algorithm.

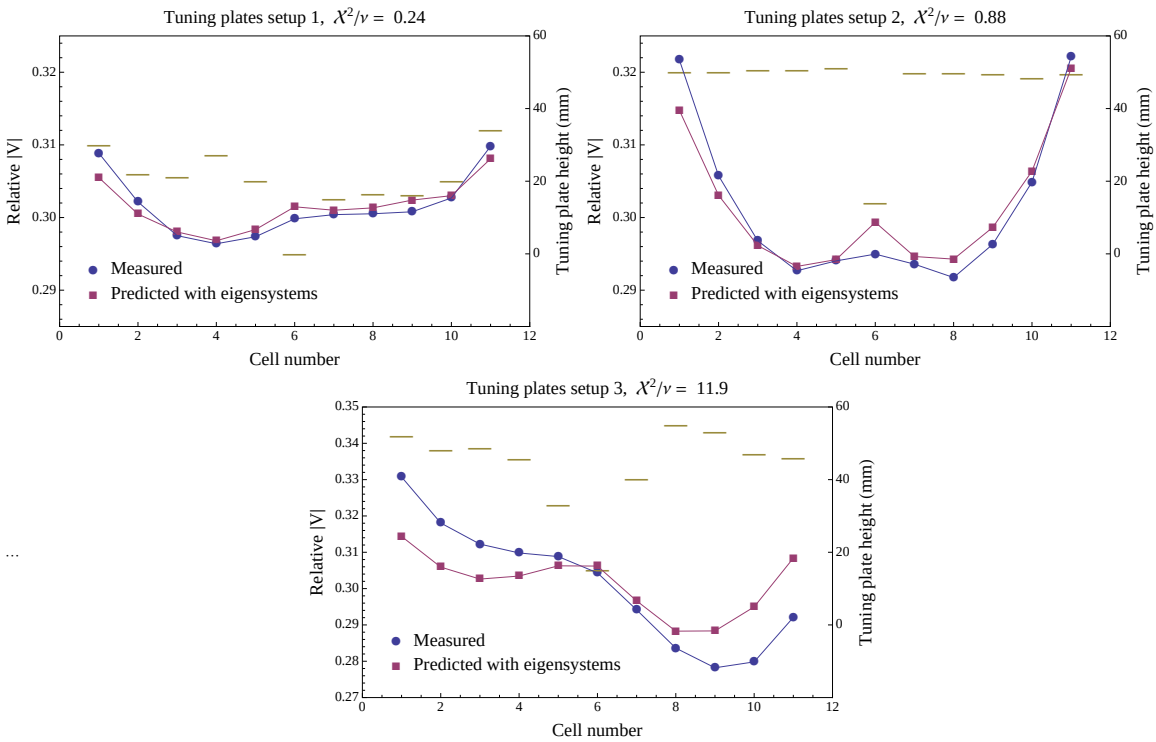

FIG. 15. The comparison between our model predictions and measurements for three different tuning plates setups are shown here. The "–" in these graphs show the tuning plate heights. And because $\chi^2/\nu < \chi^2/\nu_{\text{crit}} = 1.78$ for setups 1 and 2, the model matches the measurements. But $\chi^2/\nu \gg 1$ in setup 3 and the model prediction is unacceptable although the shape of the profile does mimic the measurement.

VII. CONCLUSION

We have shown how the application of perturbation theory to the lumped circuit model can be used to understand the physics of field flatness tuning. And because the numerical solution of eigensystems is very fast, the model also provides the opportunity for real-time calculation of the field flatness profile. When we couple the real-time calculation with an iterative process of prediction and correction, the model can be quickly refined to give

accurate results. This procedure makes it possible for the RFQ expert to not only use the model to tune the field flatness to some tolerance but also to shape it. This would be desirable because there are CST Particle Studio® simulations as well as PARMTEQ calculations that reveal the capture and transmission efficiency of the RFQ is impacted by the shape of the field profile [12, 17].

Of course, there are also improvements that need to be made to the model. For example, the present model does not predict the resonant frequency correctly. Currently, we are developing a LabView program that implements this model and will be used to tune newly built 4-rod RFQs.

Appendix A: Constructing the Eigenbra $\langle \boldsymbol{J}_k|$

Let us write down the eigenvectors $\boldsymbol{J}_k$ of $\boldsymbol{U}_0(\kappa_1, 0)$ as eigenkets, i.e.

$$\boldsymbol{J}_k = |\Lambda_k\rangle \tag{A1}$$

Unfortunately, $\{|\Lambda_k\rangle|\ k = 0, \ldots, N\}$ do not form an orthonormal set because $\boldsymbol{U}_0(\kappa_1, 0)$ is not symmetric. However, we can always construct a set of eigenbras $\{\langle\Lambda_k||\ k = 0, \ldots, N\}$ that are orthogonal to $\{|\Lambda_k\rangle|\ k = 0, \ldots, N\}$ *if* its eigenvalues are distinct. In this paper, it is, indeed, the case from Eq. 16.

We start with the similarity transformation that diagonalizes $\boldsymbol{U}_0(\kappa_1, 0)$ from Eq. 15

$$\begin{aligned} &\underline{\boldsymbol{J}}^{-1}\boldsymbol{U}_0(\kappa_1, 0)\underline{\boldsymbol{J}} = \boldsymbol{\Lambda} \\ \Rightarrow \quad &\boldsymbol{U}_0(\kappa_1, 0)\underline{\boldsymbol{J}} = \underline{\boldsymbol{J}}\boldsymbol{\Lambda} \quad \text{and} \quad \underline{\boldsymbol{J}}^{-1}\boldsymbol{U}_0(\kappa_1, 0) = \boldsymbol{\Lambda}\underline{\boldsymbol{J}}^{-1} \end{aligned} \tag{A2}$$

Therefore, from the last line of Eq. A2, we can see that the $(k+1)$'th column of $\underline{\boldsymbol{J}}$ is the right eigenvector of $\boldsymbol{U}_0(\kappa_1, 0)$ associated with eigenvalue Λ_k and the $(k+1)$'th row vector of $\underline{\boldsymbol{J}}^{-1}$ is the left eigenvector of $\boldsymbol{U}_0(\kappa_1, 0)$ associated with the same eigenvalue Λ_k.

Hence, if we define $(\boldsymbol{J}^{-1})_k$ to be the $(k+1)$'th row of $\underline{\boldsymbol{J}}^{-1}$, we can write

$$(\boldsymbol{J}^{-1})_k = \langle\Lambda_k| \tag{A3}$$

and it is clear from $\underline{\boldsymbol{J}}^{-1}\underline{\boldsymbol{J}} = \boldsymbol{I}$ so that

$$\langle\Lambda_k|\Lambda_\ell\rangle = (\boldsymbol{J}^{-1})_k\boldsymbol{J}_\ell = \delta_{k\ell} \tag{A4}$$

where $\delta_{k\ell}$ is the Kronecker δ.

Thus, we have found a set of eigenbras $\{\langle\Lambda_k|| \; k = 0, \ldots, N\}$ that are orthonormal to the eigenkets $\{|\Lambda_k\rangle| \; k = 0, \ldots, N\}$.

Appendix B: $\boldsymbol{J}$ and $\boldsymbol{J}^{-1}$ in matrix form

$$\underline{\boldsymbol{J}} = \begin{pmatrix} A_0 & A_1 & A_2 & \ldots & A_k & \ldots & A_N \\ A_0 & A_1 \cos\frac{\pi}{N} & A_2 \cos\frac{2\pi}{N} & \ldots & A_k \cos\frac{k\pi}{N} & \ldots & -A_N \\ A_0 & A_1 \cos\frac{2\times\pi}{N} & A_2 \cos\frac{2\times 2\pi}{N} & \ldots & A_k \cos\frac{2\times k\pi}{N} & \ldots & A_N \\ \vdots & \vdots & \vdots & & \vdots & & \vdots \\ A_0 & A_1 \cos\frac{(N-2)\pi}{N} & A_2 \cos\frac{(N-2)2\pi}{N} & \ldots & A_k \cos\frac{(N-2)k\pi}{N} & \ldots & (-1)^{N-2} A_N \\ A_0 & A_1 \cos\frac{(N-1)\pi}{N} & A_2 \cos\frac{(N-1)2\pi}{N} & \ldots & A_k \cos\frac{(N-1)k\pi}{N} & \ldots & (-1)^{N-1} A_N \\ A_0 & -A_1 & A_2 & \ldots & (-1)^k A_k & \ldots & (-1)^N A_N \end{pmatrix} \tag{B1}$$

$$\underline{\boldsymbol{J}}^{-1} = \begin{pmatrix} \frac{1}{2NA_0} & \frac{1}{NA_0} & \frac{1}{NA_0} & \ldots & \frac{1}{NA_0} & \frac{1}{2NA_0} \\ \frac{1}{NA_1} & \frac{2}{NA_1} \cos\frac{1\times\pi}{N} & \frac{2}{NA_1} \cos\frac{2\times\pi}{N} & \ldots & \frac{2}{NA_1} \cos\frac{(N-1)\pi}{N} & -\frac{1}{NA_1} \\ \frac{1}{NA_2} & \frac{2}{NA_2} \cos\frac{1\times 2\pi}{N} & \frac{2}{NA_2} \cos\frac{2\times 2\pi}{N} & \ldots & \frac{2}{NA_2} \cos\frac{(N-1)\times 2\pi}{N} & \frac{1}{NA_2} \\ \vdots & \vdots & \vdots & & \vdots & \vdots \\ \frac{1}{NA_k} & \frac{2}{NA_k} \cos\frac{1\times k\pi}{N} & \frac{2}{NA_k} \cos\frac{2\times k\pi}{N} & \ldots & \frac{2}{NA_k} \cos\frac{(N-1)k\pi}{N} & \frac{(-1)^k}{NA_k} \\ \vdots & \vdots & \vdots & & \vdots & \vdots \\ \frac{1}{2NA_N} & -\frac{1}{NA_N} & \frac{1}{NA_N} & \ldots & \frac{(-1)^{N-1}}{NA_N} & \frac{(-1)^N}{2NA_N} \end{pmatrix} \tag{B2}$$

Appendix C: Modes calculated by CST

From our calculations discussed in section II, we know that for $(N+1)$ tuning cells, there are $(N+1)$ possible modes. One way to number these modes is to look at the E-field phase shift per tuning cell

$$\varphi = q\pi/N \tag{C1}$$

where $q = 0, 1, \ldots, N$, as it can also be found in [18] for example. Here, we can interpret q as the quantum number that tells us the number of cells where the E-field is zero, i.e. the number of nodes. We can identify the mode id's used in our paper, which are based on the

current distribution and therefore are magnetic modes, i.e. H-modes. We will denote them as mode_H here. The relationship between q and mode_E and mode_H is given below:

$$\text{mode}_E = \frac{q\pi}{N}, \qquad \text{mode}_H = \frac{(N-q)\pi}{N} \tag{C2}$$

We illustrate the phase shift φ using the FNAL RFQ as an example. We find that the lowest mode found by MWS is 152.9 MHz and the next higher mode is 192.1 MHz, which are both quadrupole modes. For these two modes, the normal E-field components on the electrodes calculated by MWS are shown in Fig. 16(a) for $\text{mode}_E = 0$ and (c) with $\text{mode}_E = 1\pi/12$. The corresponding currents on the stems are shown in Fig. 16(b) and (d). As a comparison, we can see that for $\text{mode}_E = 0$, the current distributions flow in opposite directions between adjacent tuning cells corresponding to $\text{mode}_H = \pi$ which is exactly like what we had described in Fig. 6. This fundamental mode of the 4-rod-RFQ is used as the operating mode and is called the $\pi - 0$ mode.

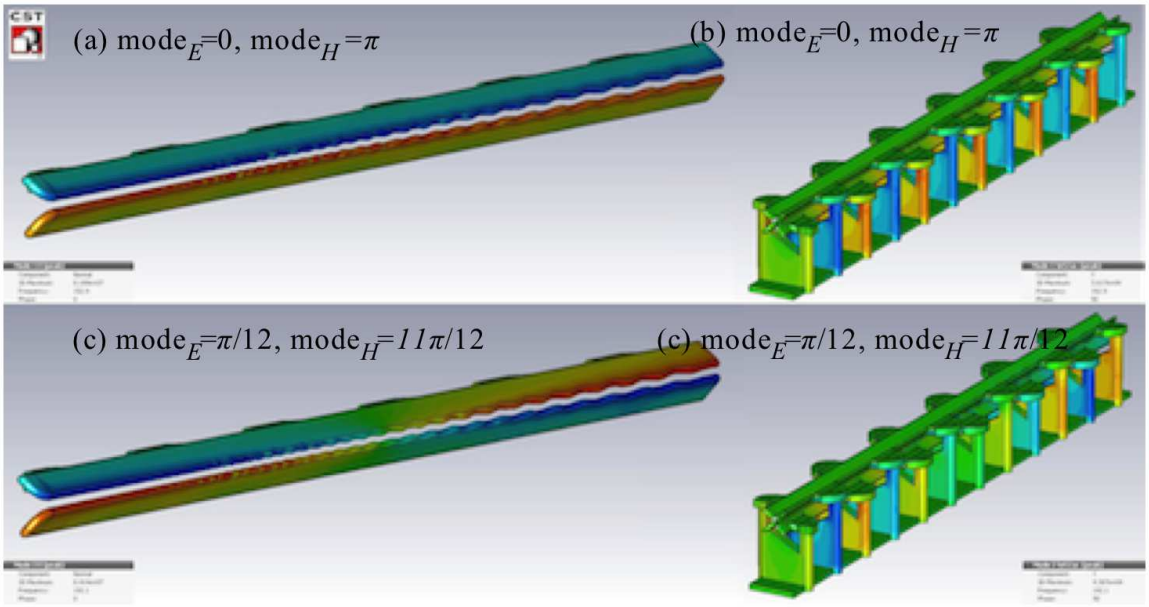

FIG. 16. The FNAL RFQ normal E-field component on the electrodes of the first two modes are shown in (a) and (c) and their corresponding currents on the stems are shown in (b) and (d). Both modes are quadrupole modes. The first mode has a constant E-field ($q = 0$) while the second mode shows one change in the field polarity ($q = 1$) along the structure. The quadrupole mode of the E-field is $\text{mode}_E = 0$ in the fundamental state with the corresponding H-field having $\text{mode}_H = \pi$. The highest quadrupole mode for the 4-rod RFQ is $\text{mode}_E = \pi$ with $\text{mode}_H = 0$ combination.

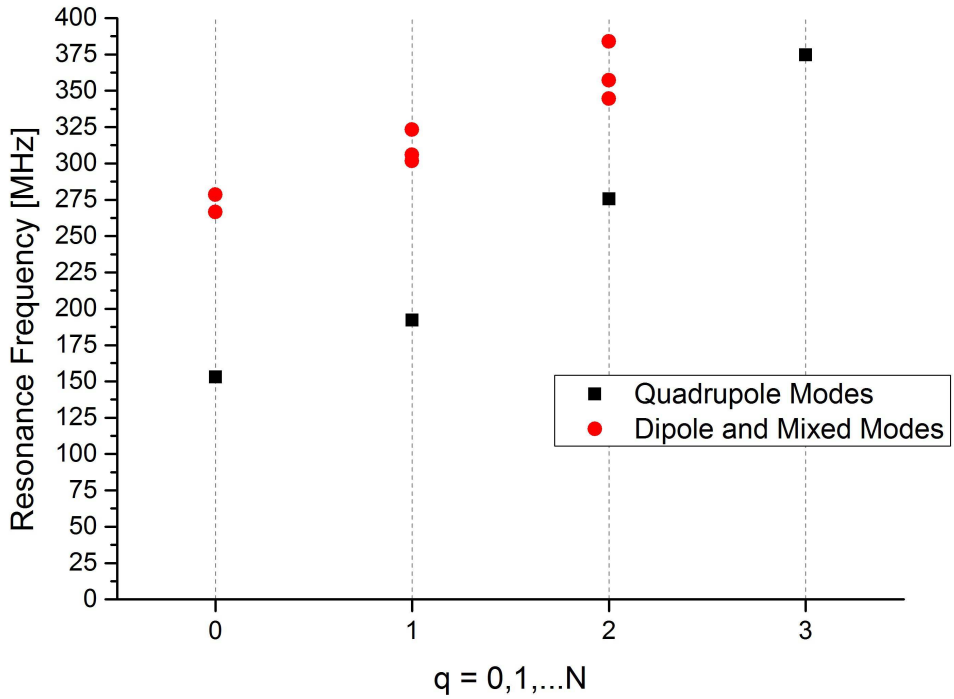

FIG. 17. The dispersion relation of the FNAL RFQ up to 400 MHz calculated by MWS. The first two modes are quadrupole modes and the first dipole like mode can be found at about 125 MHz above the operating mode.

The dispersion diagram up to 400 MHz of the FNAL RFQ without any tuning is given in Fig. 17. It includes all modes simulated by MWS. Due to the connection of the electrodes to the stems, the higher order modes are far away from the fundamental mode, $q = 0$, where the RFQ operates. The spectrum is grouped into transverse quadrupole modes (black "■") and the dipole and mixed modes (red "●"). Sometimes, the dipole and higher order transverse modes in the simulation results are hard to distinguish. In the 4-rod RFQ, the fundamental mode of the E-field is always the quadrupole mode with a constant E-field ($q = 0$) along the structure. The next mode is also a quadrupole mode, but the potential on the electrodes changes sign once along the structure, a $q = 1$ state. This mode is already 40 MHz higher than the operating mode without any tuning. The first mode that shows a dipole like potential distribution with a constant field along the structure is about 125 MHz higher compared to the operating mode. Note: the weakness of our model mentioned in

section III B 3 also manifests itself in predicting higher order eigenfrequencies that are too small.

ACKNOWLEDGMENTS

We would like to thank R. Madrak for proof reading our manuscript. And this work is supported by Fermi Research Alliance, LLC under Contract No. DE-AC02-07CH11359 with the United States Department of Energy and the Bundesministerium für Bildung und Forschung (BMBF).

---

[1] P. Fischer and A. Schempp. Tuning of a 4-rod CW-mode RFQ accelerator. In C. Biscari et al., editors, *Proc. EPAC 2006, Edinburgh, Scotland, 26–30 Jun 2006*, pages 1583–1585, 2006.

[2] J. Schmidt et al. Simulations of the influence of 4-rod RFQ elements on its voltage distribution. In J. Corbett et al., editors, *Proc. IPAC 2012, New Orleans, Louisiana, 20–25 May 2012*, pages 3818–3820, 2012.

[3] J. Schmidt et al. Tuning studies on 4-rod RFQs. In *Proc. Linac 2012, Tel Aviv, Israel, 09–14 Sep 2012*, 2012.

[4] H. Podlech et al. Electrodynamic calculations of the 4-rod-RFQ resonator for the Heidelberg high current injector. In *Proc. PAC 2001, Chicago, USA*, pages 3069–3071, 2001.

[5] S. Kurennoy, R.W. Gernett, and L.J. Rybarcyk. Electromagnetic and multi-particle beam dynamics modeling of 4-rod RFQs. In *Proc. IPAC 2013, Shanghai, China*, pages 3978–3980, 2013.

[6] A. Schempp et al. Zero-mode-RFQ development in Frankfurt. In U. Grundinger et al., editors, *Proc. LINAC 1984, Darmstadt, Germany, 07–11 May 1984*, pages 100–102, 1984.

[7] V. Kapin. A new analysis of 4-rod radio-frequency quadrupole linac with intrinsic field distortions. *Jpn. J. Appl. Phys.*, 36(Part 1, 4A):2415–2427, April 1997.

[8] A. Palmieri et al. Perturbation analysis on a four-vane RFQ. In A. Noda et al., editors, *Proc. IPAC 2010, Kyoto, Japan, 23–28 May 2010*, pages 606–608, 2010.

[9] J.X. Fang and A. Schempp. Equivalent circuit of a 4-rod RFQ. In J. Corbett et al., editors, *Proc. EPAC 1992, Berlin, Germany, 24–28 Mar 1992*, pages 1331–1333, 1992.

[10] Intuitively, we can imagine that κ_1 and κ_2 can be different between cells even when the tuning plates are at the same height. However, when we look at Fig. 9, we see the MWS data can be well fitted with only two coupling constants κ_1 and κ_2.

[11] W.H. Hayt and J.E. Kemmerly. *Engineering Circuit Analysis, 4th Edition.* McGraw-Hill Book Company, 1986.

[12] P. Fischer. *Ein Hochleistungs-RFQ-Beschleuniger füer Deuteronen.* PhD thesis, IAP, Goethe University, Frankfurt am Main, 2007.

[13] C.Y. Tan et al. The 750 keV RFQ injector upgrade. Technical Report Beams-doc-3646-v14, Fermilab, 2013.

[14] K. Küpfmüller et al. *Theoretische Elektrotechnik.* Springer, 2008.

[15] Some details about how, in general, the measurements are done can be found in references [2, 3, 12]. The FNAL RFQ measurements are documented in [13] section 4.3.4.

[16] P. Bevington and D.K. Robinson. *Data Reduction and Error Analysis for the Physical Sciences.* McGraw-Hill Book Company, 2002.

[17] S. Kurennoy. CST results: transmission vs. V profile at fixed V_{av}. private communication, 2012.

[18] M. Vretenar. Low-beta structures. In *CAS - RF for accelerators, Ebeltoft, Denmark, 2010*, 2010.